(Received 12 March 2026, Accepted 16 April 2026, Scheduled 10 May 2026)

EM Field Comparison of Five Lightning Types: A Distance-Dependent Behavior with Implications for Protection Design

Imane Ghlib, Mohamed Omari*, and Abdenbi Mimouni

Laboratory of Electrical Engineering and Plasmas, University of Tiaret, Tiaret 14000, Algeria

ABSTRACT: Lightning electromagnetic fields are essential inputs for protection system design, electromagnetic compatibility analysis, and lightning location system calibration. Although most computational studies rely on a single "typical" current waveform, real lightning exhibits significant variation in peak current, rise time, and temporal characteristics. This paper presents a systematic investigation of how return stroke current parameters influence radiated electromagnetic fields using the finite-difference time-domain (FDTD) method. Five representative waveforms are examined: typical subsequent stroke (12 kA, 40 kA/µs), first return stroke (28 kA, 12 kA/µs), severe subsequent stroke (25 kA, 80 kA/µs), fast-rising subsequent stroke (20 kA, 120 kA/µs), and rocket-triggered lightning (16 kA, 20 kA/µs). Simulations are performed over homogeneous ground ($\sigma = 0.001$ S/m, $\varepsilon_r = 10$). Electric and magnetic field components are computed at near-field ($r = 50$ m) and far-field ($r = 5$ km) distances, both underground ($d = 2$ m) and above ground ($h = 10$ m). Results show strongly distance-dependent behavior: at 50 m, current rise rate (di/dt) dominates, with fast-rising 16 kA strokes producing fields comparable to slower 22 kA events. At 5 km, peak current governs all components, with 28 kA first strokes producing fields 1.5–2× higher than subsequent strokes. Field attenuation from 50 m to 5 km varies from 130× to 3000× depending on waveform frequency content. The azimuthal magnetic field exhibits uniform attenuation (225–350×) and ground independence, supporting its use in lightning location systems. Triggered lightning underestimates severe natural strokes by 40–60% at 50 m, narrowing to 20–30% at 5 km. These findings indicate that worst-case protection scenarios must be distance-specific: fast-rising strokes govern buried infrastructure within 100 m, while first strokes dominate overhead systems beyond 1 km.

1. INTRODUCTION

Lightning discharges are among the most powerful natural sources of electromagnetic transients, generating intense electric and magnetic fields that can propagate over distances exceeding hundreds of kilometers [1]. These electromagnetic fields are critical inputs for multiple applications, serving as the basis for lightning location systems (LLSs) used worldwide for real-time lightning detection and warning [2]. They determine the severity of lightning-induced voltages on power and telecommunication lines, and govern the electromagnetic stress experienced by sensitive electronic equipment and protection systems [3–7]. Consequently, the accurate prediction of lightning electromagnetic fields is essential for lightning protection system design, electromagnetic compatibility (EMC) analysis, and the risk assessment of electrical infrastructure [8–12].

The electromagnetic fields radiated by lightning return strokes depend on two primary factors: the characteristics of the lightning current and the electrical properties of the propagation medium. Extensive research has been devoted to understanding the influence of ground conductivity and soil stratification on field propagation [13–15]. More recent studies have demonstrated that vertical soil stratification [16], mixed propagation paths, such as land-ocean interfaces [17], and frequency-dependent soil parameters [18] can significantly alter electromagnetic field characteristics, particularly at intermediate and far distances from lightning channels.

While soil and propagation effects have been extensively studied, considerably less attention has been devoted to systematically investigating how variations in lightning current characteristics influence the resulting electromagnetic fields. Most computational studies employ a single "typical" current waveform, often a subsequent return stroke with a peak current of approximately 10–12 kA [19], without examining the sensitivity of field predictions to current parameter variations. However, natural lightning exhibits wide variability: first return strokes typically feature peak currents of 25–30 kA with relatively slow rise times (10–15 kA/µs), while subsequent strokes show lower peaks (10–15 kA) but much faster rise rates (40–100 kA/µs or higher) [20, 21]. Furthermore, rocket-triggered lightning, which is increasingly used for controlled experiments and protection system validation [18–22], displays distinctly different temporal characteristics from those of natural lightning. Understanding how these variations in the current waveform affect the severity of the electromagnetic field is crucial for several reasons: protection standards must account for the range of possible lightning characteristics, electromagnetic compatibility assessments require knowledge of worst-case field scenarios, and the validity of using triggered lightning as a surrogate for natural events must be quantified.

* Corresponding author: Mohamed Omari (mohamed.omari@univ-tiaret.dz).

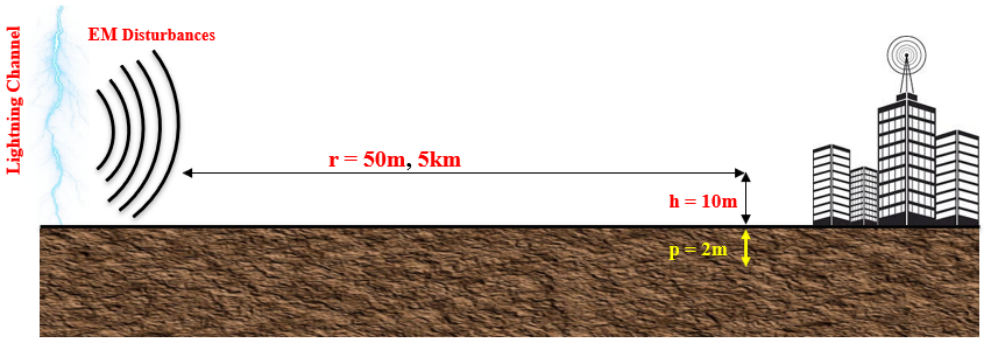

FIGURE 1. The adopted problem geometry.

Although several studies have touched upon the effects of current waveform, no comprehensive study has systematically compared electromagnetic fields across the full spectrum of lightning types under controlled conditions. This gap has critical implications for protection system design, as current standards often specify single "worst-case" scenarios without recognizing that different infrastructures at different distances may experience peak stress from fundamentally different lightning characteristics. Buried cables within 100 m may be most vulnerable to fast-rising strokes (extreme di/dt), whereas overhead lines at kilometer distances may experience maximum stress from the first return strokes (sustained high fields). Without a systematic distance-dependent comparison, protection designs risk over-engineering (excessive cost) or under-protection (safety hazards). This study addresses this gap through systematic FDTD simulations by examining five representative waveforms: typical subsequent stroke (12 kA, 40 kA/µs baseline), first stroke (28 kA, 12 kA/µs high-energy), severe subsequent stroke (25 kA, 80 kA/µs), fast-rising subsequent stroke (20 kA, 120 kA/µs worst-case EMI), and triggered lightning (16 kA, 20 kA/µs controlled experimental). Simulations over a homogeneous ground ($\sigma = 0.001$ S/m, $\varepsilon_r = 10$) compute three field components at two critical distances: $r = 50$ m (near-field, maximum coupling to buried cables and nearby structures) and $r = 5$ km (far-field, regional grounding networks and transmission corridors), with fields evaluated underground ($p = 2$ m, buried infrastructure) and above ground ($h = 10$ m, overhead lines). This dual-distance approach enables the identification of distance-dependent worst-case scenarios, which are essential for developing cost-effective, risk-informed protection guidelines based on field exposure levels, ensuring safety without unnecessary over-specification.

2. THE ADOPTED MODELS AND APPROACHES

2.1. The Problem Geometry and Simulation Setup

Figure 1 illustrates the computational geometry adopted in this study. A vertical lightning channel strikes a homogeneous ground, and electromagnetic fields are computed at a horizontal distance of $r = 50$ m from the channel base at two vertical positions: $h = 10$ m above ground level, representing overhead power lines and telecommunication cables, and $p = 2$ m below ground level, representing buried infrastructure such as underground power cables, water pipes, and grounding systems.

The electromagnetic field components are computed using the two-dimensional cylindrical finite-difference time-domain (FDTD) method in the (r, z) plane, exploiting the axial symmetry of the problem. The computational domain extended 3 km in both the horizontal and vertical directions above the ground, with an additional 100 m below the ground to capture the subsurface field behavior. A uniform spatial discretization of $\Delta r = \Delta z = 1$ m was employed in both the radial and vertical directions, with a time step of $\Delta t = 1$ ns, satisfying the Courant-Friedrichs-Lewy (CFL) stability condition [23].

First-order Mur absorbing boundary conditions [24] were implemented at the outer boundaries of the computational domain to minimize non-physical reflections.

The ground is modeled as a homogeneous lossy dielectric half-space with conductivity $\sigma = 0.001$ S/m and relative permittivity $\varepsilon_r = 10$, which is representative of typical dry to moderately dry soil conditions. These parameters correspond to agricultural land or dry sandy soil with approximately 2–3% water content [25]. The air above the ground is treated as lossless ($\sigma = 0$ S/m, $\varepsilon_r = 1$). This homogeneous soil configuration was deliberately chosen to isolate the influence of lightning current characteristics on electromagnetic fields without the confounding effects of soil stratification or mixed propagation paths. It is also acknowledged that the soil parameters ($\sigma = 0.001$ S/m, $\varepsilon_r = 10$) are treated as frequency-independent, which is a simplification of real soil behavior. In practice, both conductivity and permittivity increase at high frequencies as described by the Alipio-Visacro model [25].

This study focuses exclusively on radiated electromagnetic fields and their associated induced effects; direct lightning strikes and conducted current phenomena are outside the scope of this work.

2.2. FDTD-Based Modeling of Lightning Electromagnetic Fields

In the FDTD framework, Maxwell's curl equations are discretized on a staggered grid following the Yee algorithm [23]. In a two-dimensional cylindrical coordinate system, the three non-zero field components are the radial electric field E_r, vertical electric field E_z, and azimuthal magnetic field H_φ. The

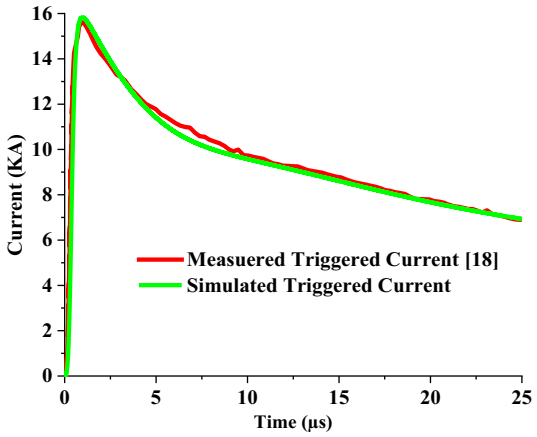

FIGURE 2. The simulated triggered lightning waveform (Case 5) is compared with the measured current from rocket-triggered lightning flash F20140603 recorded at the GCOELD facility in Conghua, China, on June 3, 2014 [18].

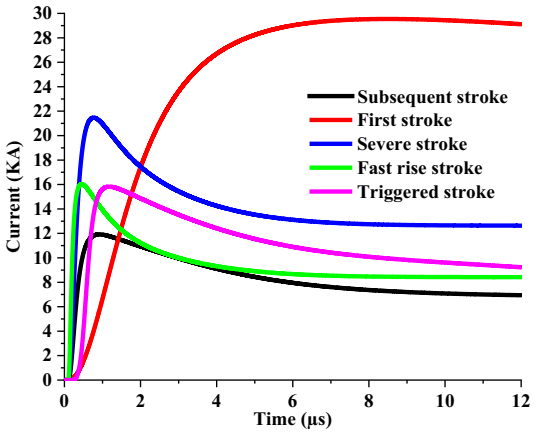

FIGURE 3. The Temporal evolution of the channel-base current $i_0(t)$ for the five examined lightning scenarios.

governing update equations are [14, 17].

$$E_z^{n+1}(i,j+1/2) = \frac{2\varepsilon-\sigma\Delta t}{2\varepsilon+\Delta t}E_z^n\left(i,j+\frac{1}{2}\right) + \frac{2\Delta t}{(2\varepsilon+\sigma\Delta t)\,ri\Delta r}\left[\begin{array}{l} r_{i+(\frac{1}{2})}H_\varphi^{n+\frac{1}{2}}\left(i+\frac{1}{2},j+\frac{1}{2}\right) \\ -r_{i-(\frac{1}{2})}H_\varphi^{n+\frac{1}{2}}\left(i-\frac{1}{2},j+\frac{1}{2}\right)\end{array}\right] \quad (1)$$

$$E_r^{n+1}(i+1/2,j) = \frac{2\varepsilon-\sigma\Delta t}{2\varepsilon+\Delta t}E_r^n\left(i+\frac{1}{2},j\right) - \frac{2\Delta t}{(2\varepsilon+\sigma\Delta t)\,\Delta r}\left[\begin{array}{l} H_\varphi^{n+\frac{1}{2}}\left(i+\frac{1}{2},j+\frac{1}{2}\right) \\ -H_\varphi^{n+\frac{1}{2}}\left(i+\frac{1}{2},j-\frac{1}{2}\right)\end{array}\right] \quad (2)$$

$$H_\varphi^{n+\frac{1}{2}}\left(i+\frac{1}{2},j+\frac{1}{2}\right) = H_\varphi^{n-\frac{1}{2}}\left(i+\frac{1}{2},j+\frac{1}{2}\right) + \frac{\Delta t}{\mu\Delta r}\left[E_z^n\left(i+1,j+\frac{1}{2}\right) - E_z^n(i,j+\frac{1}{2})\right] - \frac{\Delta t}{\mu\Delta z}\left[E_r^n\left(i+\frac{1}{2},j+1\right) - E_r^n\left(i+\frac{1}{2},j\right)\right] \quad (3)$$

where the superscripts n denote the time step; the subscripts (i,j) denote the spatial grid indices; ε is the permittivity; σ is the conductivity; and μ is the permeability of the medium at each grid point.

2.3. Lightning Source: Heidler Base Waveform and MTLE Channel Model

The lightning channel base current was modeled using a double Heidler function [26], which provides an accurate analytical representation of the measured lightning current waveforms:

$$i_0(t) = \frac{I_{01}}{\eta_1}\frac{\left(\frac{t}{\tau_{11}}\right)^2}{1+\left(\frac{t}{\tau_{11}}\right)^2}e^{\frac{-t}{\tau_{21}}} + \frac{I_{02}}{\eta_2}\frac{\left(\frac{t}{\tau_{12}}\right)^2}{1+\left(\frac{t}{\tau_{12}}\right)^2}e^{\frac{-t}{\tau_{22}}} \quad (4)$$

where I_{01} and I_{02} are the peak current amplitudes of the first and second Heidler components; τ_{11} and τ_{12} are the front time constants; τ_{21} and τ_{22} are the decay time constants; n_1 and n_2 are exponents controlling the waveform steepness; and η_1 and η_2 are amplitude correction factors ensuring that the maximum current equals the specified peak values.

To account for current propagation and attenuation along the vertical lightning channel, a Modified Transmission Line with Exponential decay (MTLE) model [27, 28] is employed:

$$i(z,t) = i_0\left(t-\frac{z}{v}\right)\exp\left(-\frac{z}{\lambda}\right) \quad (5)$$

where z is the height above ground along the channel; $v = 1.5\times10^8$ m/s is the return stroke velocity ($0.5c$, where c is the speed of light); and $\lambda = 2000$ m is the current decay constant. This combined Heidler-MTLE formulation provides a realistic representation of both the temporal characteristics at the channel base and the spatial distribution of the current along the channel.

The five waveforms selected for this study were chosen to span the primary documented categories of natural and triggered lightning, covering the full range from slow-rising first return strokes to extremely fast-rising subsequent strokes, as characterized in the literature [19, 20]. However, it is important to acknowledge that lightning is inherently a stochastic phenomenon, and the parameter space of natural lightning extends beyond these five representative cases. Statistical distributions of peak current and rise rate (such as those reported by CIGRE) show significant variability, and rare outlier events with parameters outside the ranges examined here do occur.

2.4. Model Validation

To validate the implementation of the Heidler-MTLE current model, the simulated triggered lightning waveform (Case 5) was compared with the measured current from rocket-triggered lightning flash F20140603 recorded at the GCOELD facility in Conghua, China, on June 3, 2014 [18]. Figure 2 presents this comparison, showing the measured current (red line) and simulated current using the Heidler function parameters specified in Table 1 (green line).

TABLE 1. The used parameters of the two Heidler's functions [18, 28].

	I_{01}	τ_{11}	τ_{12}	N_{01}	I_{02}	τ_{21}	τ_{22}	N_2
Subsequent stroke	10.7 (KA)	0.25 (μs)	2.5 (μs)	2	6.5 (KA)	2 (μs)	230 (μs)	2
First return stroke	28 (KA)	1.8 (μs)	95 (μs)	2	–	–	–	–
Severe subsequent stroke	20 (KA)	0.25 (μs)	2.0 (μs)	2	12 (KA)	2.5 (μs)	230 (μs)	2
Fast-rising subsequent stroke	15 (KA)	0.1 (μs)	2.0 (μs)	2	8 (KA)	2.5 (μs)	230 (μs)	2
Rocket-triggered lightning	16 (KA)	0.501 (μs)	9.6 (μs)	5	56 (KA)	10.0 (μs)	200.0 (μs)	3

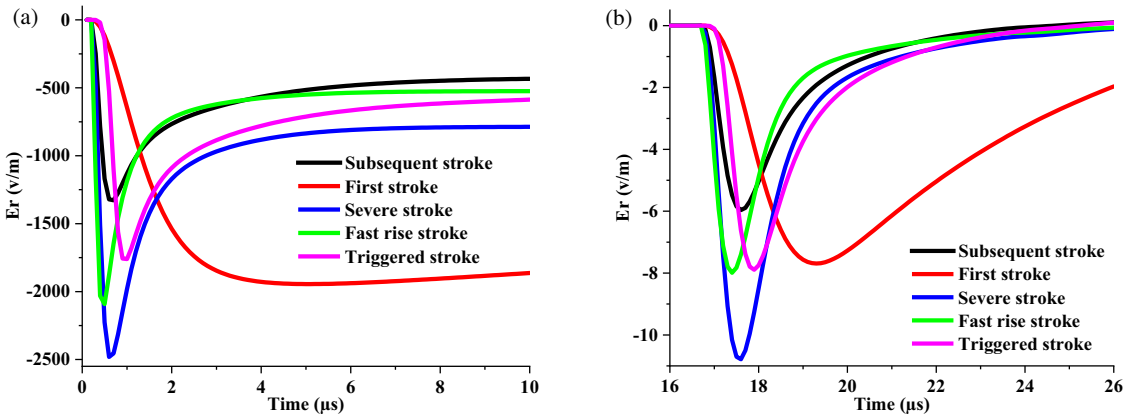

FIGURE 4. The underground ($p = 2$ m) horizontal electric field at (a) $r = 50$ m, and (b) $r = 5$ km.

The simulated waveform exhibits excellent agreement with the experimental measurement throughout the entire 25 μs time window. Both curves show a peak current of approximately 16 kA occurring at $t \approx 1$ μs, followed by a gradual decay. At $t = 5$ μs, both the measured and simulated currents reached approximately 12 kA, maintaining close agreement through the intermediate time range. By $t = 25$ μs, both waveforms decay to approximately 7 kA. The root-mean-square deviation between the measured and simulated waveforms over the 0–25 μs interval was less than 5%, confirming the accuracy of the analytical representation.

This validation demonstrates that the adopted Heidler function parameters accurately reproduce the temporal characteristics of the measured triggered lightning currents, providing confidence in the electromagnetic field predictions. The agreement also validates the overall implementation of the current source model in the FDTD code, as any errors in the Heidler function evaluation or MTLE propagation would manifest as discrepancies in this comparison.

3. RESULTS AND DISCUSSION

This section presents the computed electromagnetic field components for all five lightning scenarios, organized by field type and observation location.

Figure 3 presents the temporal evolution of the channel-base current for all five scenarios over 12 μs, revealing distinct lightning type characteristics.

Case 2 (first stroke, red) dominates with a 28 kA peak at $t \approx 5$ μs and a sustained plateau above 26 kA throughout the window, reflecting its long decay constant ($\tau_{12} = 95$ μs) and high charge transfer characteristic of first strokes. Subsequent stroke Cases (1, 3, 4) exhibit fast-rise and rapid-decay signatures. Case 3 (severe subsequent, blue) reaches 22 kA in 0.3 μs (80 kA/μs di/dt) then decays to 13 kA by 12 μs. Case 4 (fast-rising, green) shows the steepest initial slope, peaking at 16 kA in $<$ 0.2 μs (120 kA/μs di/dt) — critical for electromagnetic coupling, where induced voltages scale with di/dt — then rapidly decay to 7 kA. Case 1 (baseline subsequent, black) peaks at approximately 10 kA at 0.5 μs, exceeding the nominal 12 kA owing to the constructive superposition of dual Heidler components, and then decays to 7 kA. Triggered lightning (Case 5, magenta) displays intermediate behavior: 16 kA peak at 1 μs with moderate 20 kA/μs rise, decaying to 9 kA — faster than Case 1 despite its higher peak current, owing to shorter decay constants that reflect the different physical mechanisms governing upward-propagating triggered versus downward natural leaders.

3.1. The Horizontal Electric Field

Figure 4 presents the temporal evolution of the underground radial electric field E_r at $p = 2$ m depth for two observation distances: (a) $r = 50$ m representing near-field conditions, and (b) $r = 5$ km representing far-field conditions. At both distances, all five cases exhibited strong negative polarity with distinct temporal characteristics reflecting the interplay between the current magnitude, rise rate, and propagation distance.

At $r = 50$ m (near-field), sharp initial peaks occurred within the first 0.5 μs, followed by a rapid decay toward quasi-static values. Case 2 (first stroke) produces the largest peak mag-

nitude of approximately -1800 V/m at $t \approx 4$ µs, reflecting its highest peak current of 28 kA. The severe subsequent stroke (Case 3) generated -2500 V/m, whereas the fast-rising stroke (Case 4) produced -2100 V/m despite having 30% lower than that of Case 3. This near-equivalence demonstrates that the current rise rate (di/dt) dominates the initial underground field transient: Case 4's extremely fast rise (120 kA/µs) nearly compensates for its lower peak, producing 90% of Case 3's magnitude (80 kA/µs). Triggered lightning (Case 5) generates -1750 V/m, whereas the baseline subsequent stroke (Case 1) produced -1300 V/m. Case 4 exhibits the fastest rise time (~ 0.2 µs), directly reflecting its highest di/dt and making it particularly critical for electromagnetic coupling to buried cables and grounding systems, where induced voltages scale with the field variation rate. After approximately 2 µs, the waveform behavior converged, and the late-time field levels were governed primarily by the peak current magnitude rather than the rise rate, with Case 2 maintaining the most negative steady values.

At $r = 5$ km (far-field), the field magnitudes attenuate dramatically, but the relative behavior among the cases shifts significantly. Peak magnitudes decrease to approximately -11 to -5 V/m — representing attenuation factors of 130–250× compared to 50 m — with peaks occurring at substantially later times ($t \approx 16$–18 µs) due to propagation delay through lossy soil. Notably, the ordering of peak magnitudes differs markedly from the near-field: Case 3 (severe stroke, blue curve) now dominates with approximately -11 V/m, substantially exceeding all other cases which cluster between -6 to -8 V/m. This reversal demonstrates that at far distances, the peak current magnitude and charge transfer become the dominant factors, whereas the influence of di/dt diminishes. Case 4 (fast-rising stroke), which produced the second-largest near-field magnitude owing to its extreme 120 kA/µs rise rate, now generates the smallest far-field peaks (approximately -8 V/m), which is approximately the same as Case 2's magnitude. This dramatic shift occurs because lossy soil propagation acts as a low-pass filter, preferentially attenuating the high-frequency components associated with the fast rise times. The first return stroke (Case 2), with its slower rise (12 kA/µs) but sustained high current and long duration, produces field components with lower frequency content that propagate more efficiently through the lossy ground. Cases 1, 5, 4, and 3 produced intermediate far-field peaks (-6 to -11 V/m), with their relative ordering now primarily reflecting the peak current rather than di/dt. The temporal evolution at 5 km is also markedly different: rather than sharp sub-microsecond peaks, the waveforms exhibit a gradual rise over several microseconds, reach peak values around $t = 18$–20 µs, and then show a very slow decay, with some cases maintaining nearly constant negative values through $t = 26$ µs. This behavior reflects the dominance of quasi-static and low-frequency radiation field components at far distances, with near-field reactive components having decayed completely.

Distance-dependent behavior has critical implications for the protection of buried infrastructure. Near buried cables (within ~ 100 m of a strike), fast-rising subsequent strokes (Case 4) represent the worst-case scenario because of their extreme di/dt, which produce intense transient fields that couple efficiently to conductors. However, for regional grounding systems or buried networks extending to kilometer distances, first return strokes (Case 2) become the critical design case because of their superior far-field propagation and sustained high field levels. The 40–60% lower near-field magnitudes from triggered lightning (Case 5) compared to severe natural strokes suggest that laboratory tests may underestimate worst-case local stresses, this 40–60% near-field underestimation carries direct implications for lightning protection standards that were developed or calibrated using rocket-triggered lightning data. Surge immunity test waveforms derived from triggered lightning experiments may not represent the worst-case electromagnetic stress experienced by buried infrastructure located within 100 m of a natural lightning strike point. While safety factors embedded in existing standards, such as IEC 62305 and IEEE Std 1410, may partially compensate for this discrepancy, the results suggest that a dedicated re-evaluation of triggered-lightning-derived waveforms is warranted, particularly for near-field buried infrastructure applications. Standards bodies should consider whether the current test waveforms adequately bound the electromagnetic environment for this specific distance and infrastructure category. Although the far-field differences reduce to 20–30%, indicating better representativeness at distance. The attenuation factors varied from 130× (Case 2) to 250× (Cases 4–5) demonstrate that the field decay with distance is not uniform across lightning types, with high-frequency-content waveforms experiencing greater attenuation.

Figure 5 presents the above-ground radial electric field E_r at $h = 10$ m height for two observation distances: (a) $r = 50$ m and (b) $r = 5$ km. At close distances, all cases exhibited positive polarity, representing systematic polarity reversal from underground fields owing to electromagnetic boundary conditions at the air-soil interface. The temporal evolution and relative magnitudes differed significantly between the near-field and far-field regions.

At $r = 50$ m (near field), the fields show a gradual rise to maximum values at $t = 0.81.5$ µs rather than sharp submicrosecond peaks, followed by slow decay or sustained quasi-static levels. Case 2 (first stroke) dominates with an approximately $+18$ kV/m peak at $t \approx 10$ µs — substantially exceeding all other cases — and maintains high levels (> 17 kV/m) through $t = 10$ µs, reflecting the long-duration, high-charge-transfer nature of first strokes. Subsequent stroke cases (1, 3, and 4) and triggered lightning (5) produced significantly lower peaks ranging from $+4$ to $+8$ kV/m. Notably, the ordering differs from underground: Case 3 (severe subsequent, $+8$ kV/m) exceeds Cases 1 and 4 ($+4$ and $+5$ kV/m), while triggered lightning ($+6$ kV/m) produces fields comparable to natural subsequent strokes. Rise times vary from 0.4 µs (Case 4) to 6 µs (Case 2), however this has less impact on overhead line coupling than underground because 10 m elevation reduces sensitivity to the fastest transients. Peak magnitude scaling demonstrates that above-ground fields are dominated by peak current and charge transfer rather than di/dt: Case 2's 28 kA produces 2–3× higher fields than Cases 4–5 (16–20 kA) despite 10× slower rise rate.

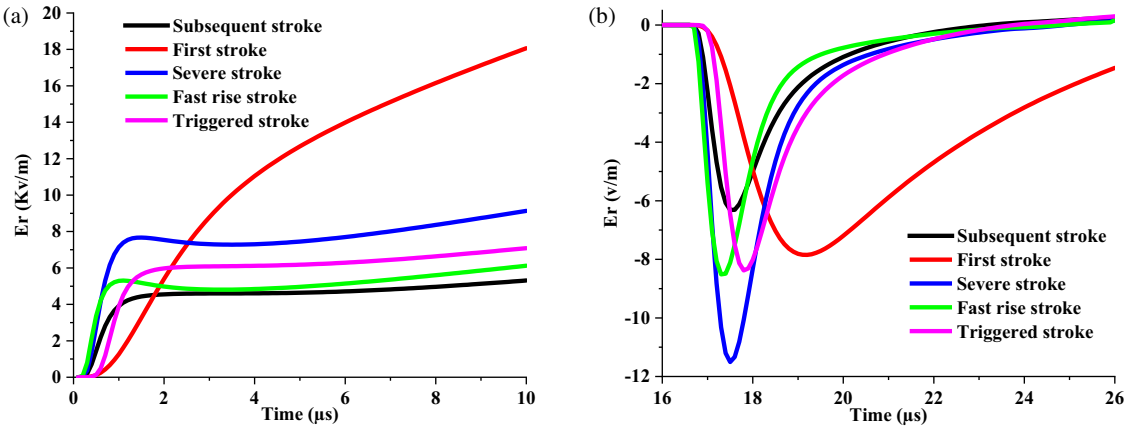

FIGURE 5. The above ground ($h = 10$ m) horizontal electric field at (a) $r = 50$ m, and (b) $r = 5$ km.

At $r = 5$ km (far-field), the field magnitudes attenuate, but the behavior shifts dramatically. Peak values decrease to approximately -12 to -6 V/m — note the polarity reversal to negative at this distance, representing attenuation factors of 1500–3000× compared to 50 m above-ground values, substantially greater than the 130–250× attenuation observed underground. Peaks occur at significantly delayed times ($t \approx 17$–18 μs) owing to propagation through air and ground. The negative polarity at 5 km indicates that at far distances above the ground, the field behavior is dominated by ground-wave propagation effects and quasi-static components that mirror the underground field polarity. Case 3 (severe stroke) was dominant with an approximately -12 V/m peak, but the margin over the other cases was reduced compared to 50 m: Cases 2, 4, and 5 clustered around -7.5 to -8.5 V/m, while Case 1 produced the smallest magnitude (-6 V/m). The convergence of Cases 1, 3, and 4 in the far field suggests that for moderate- to high-peak currents with typical subsequent stroke characteristics, the far-field above-ground radiated fields become relatively insensitive to the specific current waveform details. The dramatic polarity shift from strong positive (+18 kV/m) at 50 m to moderately negative (-12 V/m) at 5 km reflects the transition from near-field radiation and reactive components to far-field ground-wave propagation dominated by lower-frequency components that penetrate and propagate along the lossy ground surface.

Distance-dependent behavior provides several critical insights. The order-of-magnitude difference between underground (peak $\sim$ 2.5 kV/m) and above-ground (peak $\sim$ 18 kV/m) at $r = 50$ m demonstrates strong attenuation in lossy soil, providing natural shielding for buried infrastructure. However, the much greater attenuation from 50 m to 5 km above ground (1500–3000×) than underground (130–250×) indicates that above-ground fields experience more severe distance-dependent decay, likely due to ground-wave propagation losses. For overhead power line coupling at close range ($<$ 100 m), sustained high fields from first strokes (Case 2) represent the critical scenario, potentially inducing voltages exceeding equipment withstand levels over millisecond timescales. At far distances ($>$ 1 km), all lightning types produce comparable above-ground field magnitudes except for severe strokes, which maintained 1.52× higher levels. The polarity reversal between underground and above-ground fields must be considered in protection coordination: the induced voltages on the buried and overhead portions of the same conductor will have opposite polarities at 50 m, potentially creating differential stresses at the transition points, although this effect diminishes at 5 km where the polarities align.

3.2. The Vertical Electric Field

Figure 6 presents the underground vertical electric field E_z at $p = 2$ m depth for two observation distances: (a) $r = 50$ m and (b) $r = 5$ km. At both distances, all cases exhibited negative polarity with sharp initial peaks, consistent with a radial field behavior, although the relative magnitudes and temporal evolution differed significantly between the near-field and far-field regions.

At $r = 50$ m (near field), all cases produce sharp negative peaks within the first 0.5 μs. Cases 3 (severe subsequent stroke, blue curve) and 4 (fast-rising subsequent, green curve) generate the largest peaks, both reaching approximately -600 V/m at $t \approx 0.3$ μs, demonstrating their extremely high current rise rates (80 and 120 kA/μs respectively). This near-equivalence despite Case 4's lower peak current (22 kA vs 16 kA) confirms that di/dt dominates the initial vertical field transients underground. Case 5 (triggered lightning, magenta) produces approximately -400 V/m, whereas Case 1 (baseline subsequent, black) generates -300 V/m. Notably, Case 2 (first stroke, red) produced a more moderate peak of approximately -200 V/m despite having the highest peak current (28 kA), reflecting its much slower rise rate (12 kA/μs). After the initial sharp transient ($t < 1$ μs), all waveforms rapidly converged toward quasi-static values between +10 and +50 V/m — note with a polarity reversal from negative to positive — by $t = 2$ μs. This late-time positive plateau is sustained through $t = 10$ μs with minimal variation among cases, indicating that the quasi-static vertical field component underground is relatively insensitive to the specific current waveform characteristics and is governed primarily by the charge distribution along the channel. The ultra-fast rise times of Cases 3 and 4 (reaching peak within 0.5–0.3 μs) make them particularly critical for coupling to vertically oriented buried conductors, such as vertical grounding system

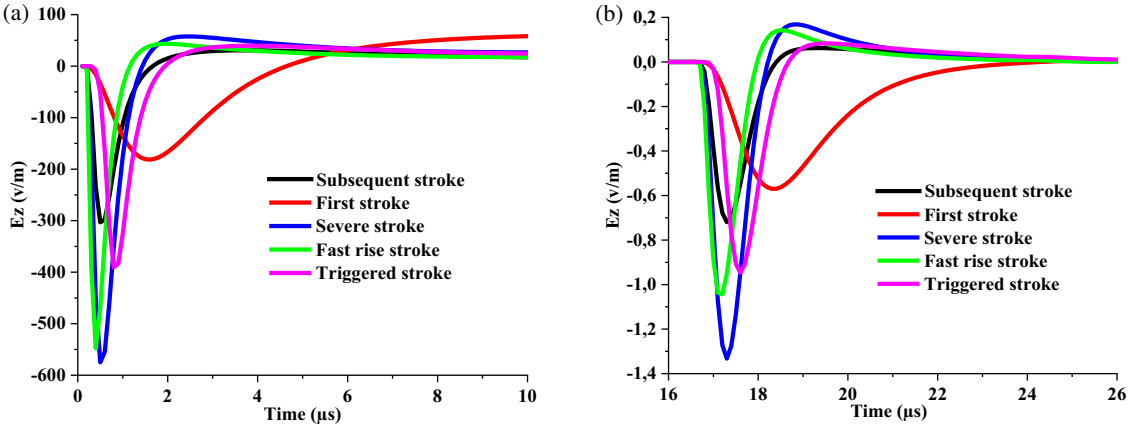

FIGURE 6. The underground ($p = 2$ m) vertical electric field at (a) $r = 50$ m, and (b) $r = 5$ km.

segments, where induced voltages are directly proportional to dEz/dt.

At $r = 5$ km (far-field), the field magnitudes attenuate substantially to approximately -1.4 to 0.2 V/m — representing attenuation factors of 200–3000× depending on the case, with peaks occurring at delayed times ($t \approx 17$–18 μs). The ordering of peak magnitudes remained as near-field: Case 3 (severe stroke) produced the largest peak magnitude of approximately -1.4 V/m, followed by Cases 4 and 5 at approximately -1 V/m, and Cases 1 and 2 at approximately -0.7 to -0.5 V/m. This preservation of ordering from 50 m to 5 km demonstrates that the vertical electric field component underground maintains di/dt sensitivity even at far distances, unlike the radial electric field which transitions to peak current dominance. However, Case 2 (first stroke) exhibits unique temporal behavior: after an initially weak peak, it undergoes a distinctive delayed descent to approximately -0.4 V/m at $t \approx 20$ μs, then maintains this sustained negative level through $t = 26$ μs. This late-time behavior reflects the long-duration, high-charge-transfer nature of the first strokes, where the cumulative quasi-static field contribution becomes significant at late times even though the initial transient response remains weak owing to the slow rise rate.

The temporal evolution at 5 km shows: rapid initial transients from high di/dt cases (Cases 3 and 4) at $t \approx 17$ μs, followed by Case 2's delayed, sustained negative field developing over longer timescales ($t = 18$–26 μs). This indicates that for the vertical electric field underground, di/dt governs the initial peak at all distances, but the peak current and charge transfer determine the late-time sustained field levels at far distances.

The distance-dependent behavior reveals critical implications for buried infrastructure protection. At both close range (50 m) and far distances (5 km), the vertical electric field component underground maintains strong di/dt sensitivity, with Cases 3 and 4 (severe and fast-rising subsequent strokes, 80–120 kA/μs) consistently producing the highest peak magnitudes at both distances. The induced voltages on vertically oriented buried conductors, such as ground rods during these fast transients (Cases 3–4 producing -600 V/m at 50 m, -1.4 to -1.1 V/m at 5 km), can potentially exceed the voltage handling capability of surge protective devices connected to the grounding system, particularly for close strikes where peak fields reach several hundred volts per meter. However, first return strokes (Case 2), despite producing the weakest initial transient peaks due to slow rise rate (12 kA/μs), exhibit unique late-time behavior at both distances: a sustained negative field, substantially exceeding the late-time levels from subsequent strokes. This indicates that while fast-rising strokes determine peak transient stress on grounding systems at all distances, first strokes create prolonged quasi-static field exposure that may govern cumulative energy dissipation and long-duration voltage stress on buried infrastructure at regional scales. The highly nonuniform attenuation, demonstrates that vertical field propagation efficiency is strongly dependent on frequency content, with high di/dt waveforms propagating their initial transients more efficiently than slow-rise waveforms. The rapid convergence to quasi-static positive values at 50 m within 2 μs, contrasted with sustained negative values at 5 km, indicates fundamentally different quasi-static field distributions at near versus far distances. For protection system design, this dual-mechanism behavior requires consideration of both fast-front transient withstand (governed by Cases 3–4 at all distances) and sustained field exposure (governed by Case 2 at far distances), as each mechanism may stress different aspects of grounding system performance — transient voltage rating versus energy absorption capacity.

Figure 7 presents the above-ground vertical electric field E_z at $h = 10$ m height for two observation distances: (a) $r = 50$ m and (b) $r = 5$ km. Unlike underground fields, all cases exhibit positive polarity at both distances, representing a systematic polarity reversal due to electromagnetic boundary conditions at the air-soil interface. The temporal evolution and relative magnitudes reveal fundamentally different behavior compared to underground fields.

At $r = 50$ m (near-field), all cases show a rapid rise within the first 2 μs followed by sustained or slowly increasing quasi-static levels through $t = 10$ μs. Case 2 (first stroke, red curve) dominates overwhelmingly, reaching approximately $+100$ kV/m by $t = 10$ μs with a continuously rising trajectory that shows no signs of saturation. This sustained growth reflects the long-duration, high-charge-transfer nature of the first strokes, where the cumulative vertical electric field continues

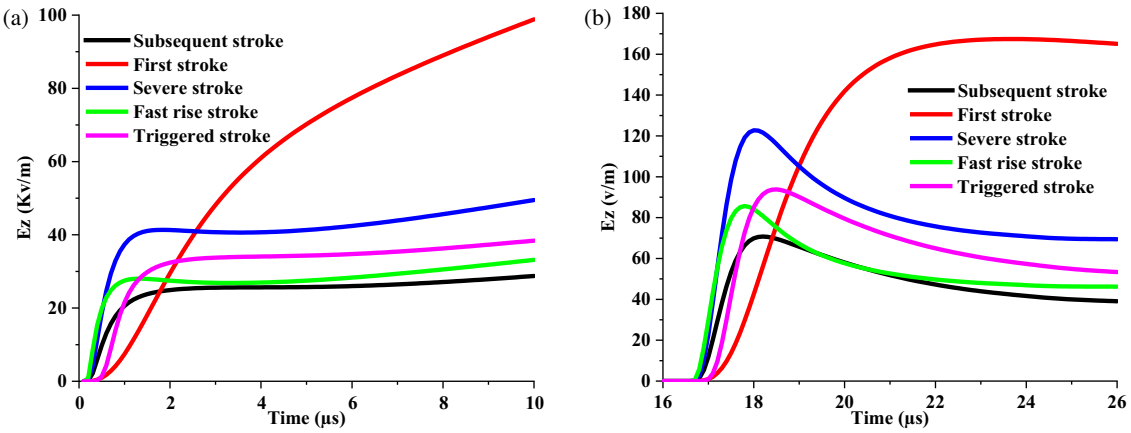

FIGURE 7. The above ground ($h = 10\,\text{m}$) vertical electric field at (a) $r = 50\,\text{m}$, and (b) $r = 5\,\text{km}$.

building as charge accumulates along the channel. Cases 3 (severe subsequent, blue) and 5 (triggered lightning, magenta) produce intermediate plateaus around +40 kV/m and +30 kV/m, respectively, reaching their peak values within 2–3 μs and then maintaining relatively constant levels. Case 1 (baseline subsequent, black) and Case 4 (fast-rising, green) generate lower quasi-static values around +25–28 kV/m. Notably, the ordering differs markedly from underground behavior: Case 2's dominance is far more pronounced (2–3× higher than other cases), and the high-di/dt Cases 3–4 do not show the superiority observed underground. Instead, peak current magnitude becomes the primary determinant of above-ground vertical field amplitude. The rapid initial rise (within 0.5–1 μs) followed by sustained high levels indicates that above-ground vertical fields are dominated by electrostatic and low-frequency radiation components rather than the high-frequency transients that characterize underground fields. This has critical implications for coupling to overhead lines: the sustained high vertical fields create prolonged electromagnetic stress on insulators and can induce significant voltages in elevated conductors through both direct coupling and via horizontal field components.

At $r = 5\,\text{km}$ (far field), the magnitudes attenuate substantially to +160 V/m (Case 2) and +65–120 V/m (others), with attenuation factors of 625× (Case 2) to 800× (other cases). Case 2 maintains dominance (+160 V/m at $t \approx 20$ μs), substantially exceeding the others, with sustained +165 V/m through 26 μs. Cases 3 and 5 generate +90–120 V/m at 17.5–18 μs, decaying to +60–80 V/m. Cases 1 and 4 produce +60–80 V/m decaying to +40–50 V/m. The temporal evolution shows far-field characteristics: rapid rise to the peak within microseconds, followed by a slow decay reflecting the efficient propagation of low-frequency content. The pronounced dominance of Case 2 (2–3× higher even at 5 km) demonstrates that first strokes maintain an electromagnetic signature across all distances for above-ground vertical fields owing to the high peak current (28 kA) and long duration. Peaks occur at later times (17–20 μs) versus underground (16–18 μs), reflecting different propagation: primarily through air versus lossy soil.

Distance-dependent behavior provides critical insights. The 625–800× attenuation from 50 m to 5 km above ground is comparable to radial field attenuation, indicating a similar distance-dependent decay. For overhead systems, sustained high vertical fields from the first strokes represent critical scenarios: +100 kV/m at 50 m and +160 V/m at 5 km create prolonged stress on insulators and can cause flashovers on transmission lines with reduced insulation. The order-of-magnitude difference between underground (peak ~ -600 V/m at 50 m) and above-ground (peak $\sim$ 100 kV/m at 50 m) — factor of approximately 170× — demonstrates dramatic field enhancement above ground owing to the absence of lossy soil attenuation. The polarity reversal between underground (negative) and above-ground (positive) must be considered for transitioning structures, although magnitude asymmetry (170× higher above ground) means above-ground fields dominate differential stress effects.

3.3. The Azimuthal Magnetic Field

Having characterized the electric field components above and below ground, we now turn to the azimuthal magnetic field H_φ — the third field component computed in this study. Figure 8 presents the underground magnetic field at $p = 2\,\text{m}$ for both near-field and far-field distances. Unlike the electric field components which exhibit polarity reversals, the magnetic field maintains a consistent positive polarity at both distances, reflecting the fundamental relationship between magnetic field circulation and current flow direction.

At $r = 50\,\text{m}$ (near-field), all cases exhibit a rapid rise to peak values within the first 0.5–1 μs, followed by gradual decay toward sustained quasi-static levels through $t = 10$ μs. Case 2 (first stroke, red curve) produces the dominant peak of approximately 90 A/m at $t \approx 8$ μs, substantially exceeding all other cases, and maintains the highest sustained level around 85–90 A/m through $t = 10$ μs. This behavior reflects the combination of high peak current (28 kA) and long-duration characteristics of first strokes. Cases 3 (severe subsequent, blue) and 5 (triggered lightning, magenta) generate intermediate peaks around 60 A/m and 45 A/m respectively, decaying to sustained levels of approximately 35–40 A/m and 30–35 A/m. Case 4 (fast-rising, green) produces a peak of approximately 40 A/m, while Case 1 (baseline, black) generates the lowest peak around 30 A/m, with both decaying to approximately 20–

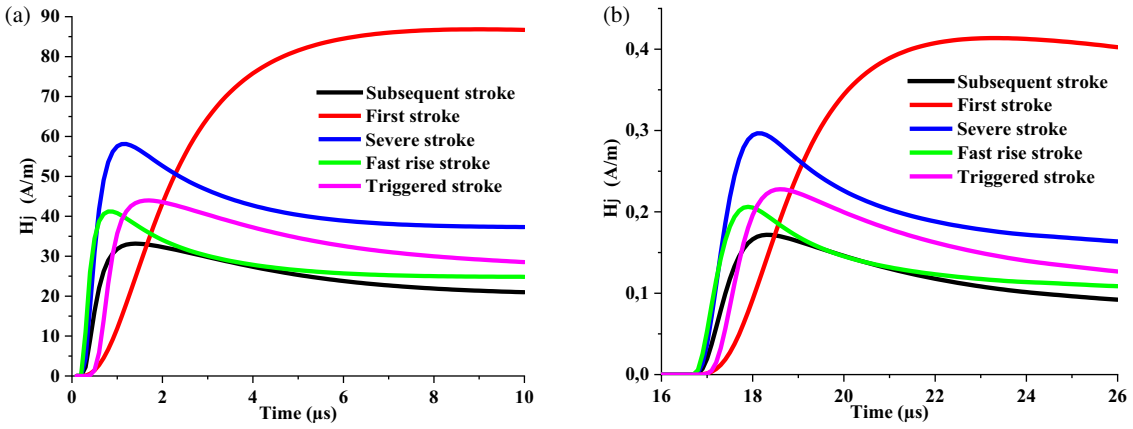

FIGURE 8. The underground ($p = 2$ m) azimuthal magnetic field at (a) $r = 50$ m, and (b) $r = 5$ km.

25 A/m by $t = 10$ μs. Notably, the ordering of peak magnitudes correlates more strongly with peak current than with di/dt: Case 2 (28 kA) > Case 3 (22 kA) > Case 5 (16 kA) ≈ Case 4 (16 kA) > Case 1 (12 kA). This indicates that unlike electric field components, which show strong di/dt dependence underground, the magnetic field component is primarily governed by peak current magnitude even at close range. The time-to-peak also varies systematically: Case 2 reaches maximum at $t \approx 8$ μs (reflecting its slower rise), while Cases 3–4 peak earlier at $t \approx 0.51$ μs (reflecting faster rise rates), and all cases then exhibit slow decay, reflecting the quasi-static magnetic field distribution around the current-carrying channel. The relatively gradual temporal evolution compared to electric field components makes the magnetic field less critical for fast transient coupling but more important for sustained electromagnetic stress and heating effects in buried metallic structures.

At $r = 5$ km (far-field), magnetic field magnitudes attenuate to approximately 0.4 to 0.15 A/m — representing attenuation factors of 225× (Case 2) to 300× (Case 1) — with peaks occurring at delayed times ($t \approx 18$–22 μs). The ordering of peak magnitudes remains consistent with near-field behavior: Case 2 (first stroke) maintains dominance with approximately 0.4 A/m, followed by Cases 3 and 5 at approximately 0.3 A/m and 0.22 A/m, and Cases 4 and 1 at approximately 0.2 and 0.18 A/m. This preservation of ordering from 50 m to 5 km — in contrast to the dramatic ordering reversals observed for electric field components — demonstrates that magnetic field magnitudes remain primarily correlated with peak current magnitude across all distance ranges, with di/dt playing a secondary role. The temporal evolution at 5 km shows characteristic far-field behavior: gradual rise over several microseconds to peaks around $t = 18$–20 μs, followed by very slow decay with Case 2 maintaining approximately 0.38 A/m through $t = 26$ μs. The attenuation factors (225–300×) are notably more uniform across cases compared to electric field components (which ranged from 130–3000×), indicating that magnetic field propagation through lossy soil is less sensitive to waveform frequency content. This occurs because the magnetic field is directly related to current magnitude through Ampère's law, and the lower frequency content associated with current magnitude variations experiences less attenuation than the higher frequency content associated with rapid current changes (di/dt) that dominate electric field behavior.

Distance-dependent behavior reveals important characteristics of the magnetic field. Uniform attenuation factors (225–300×, 33% variation) compared to electric fields (130–3000×, order-of-magnitude variation) demonstrate that the magnetic field decay is more predictable and less dependent on waveform specifics, enhancing the reliability of lightning current estimation. The consistent ordering (Case 2 > Case 3 > Case 5 ≈ Case 4 > Case 1) at both distances, correlating with the peak current, validates the magnetic field measurements for peak current estimation in lightning location systems. For buried infrastructure, magnetic fields primarily induce currents and heating rather than voltage stress. Sustained high fields from first strokes (90 A/m at 50 m, 0.4 A/m at 5 km) induce significant circulating currents in buried metallic structures (pipelines, cable sheaths, and grounding grids), potentially causing localized heating or electromagnetic interference. Magnetic fields propagate more efficiently than electric fields for high-frequency waveforms, making them valuable for characterizing fast- rising events at distances where electric fields are severely attenuated.

Figure 9 presents the above ground magnetic field at $h = 10$ m for both $r = 50$ m (a) and $r = 5$ km (b).

At $r = 50$ m (near field), all cases exhibit a rapid rise to peak values within the first 0.5–1.5 μs, followed by a gradual decay toward sustained quasi-static levels through $t = 10$ μs. Case 2 (first stroke, red curve) produces the dominant peak of approximately 95 A/m at $t \approx 5$–6 μs, maintaining the highest sustained level of approximately 90–95 A/m through $t = 10$ μs — nearly identical to the underground value (90 A/m), indicating minimal attenuation difference between above-ground and underground magnetic field propagation at close range. Cases 3 (severe subsequent, blue) and 5 (triggered lightning, magenta) generated intermediate peaks of approximately 65 A/m and 50 A/m respectively, decaying to sustained levels of approximately 45 A/m and 35 A/m. Case 4 (fast rising, green) produces a peak of approximately 45 A/m, whereas Case 1 (baseline, black) generates the lowest peak of approximately 35 A/m, with both decaying to approximately 30 A/m by $t = 10$ μs. The ordering remains consistent with the un-

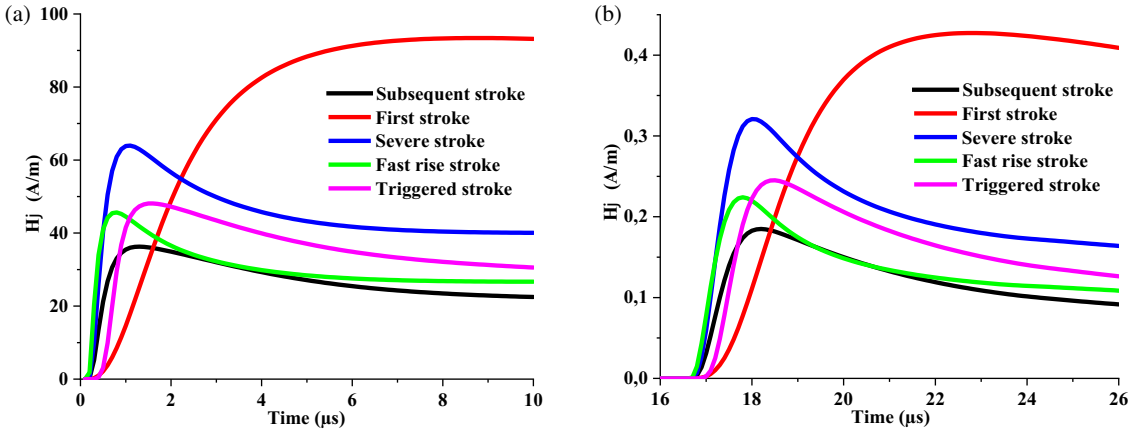

FIGURE 9. The above-ground ($h = 10$ m) azimuthal magnetic field at (a) $r = 50$ m, and (b) $r = 5$ km.

derground behavior and correlates strongly with the peak current magnitude: Case 2 (29 kA) $\gg$ Case 3 (22 kA) $>$ Case 5 (16 kA) $\approx$ Case 4 (16 kA) $>$ Case 1 (12 kA). The remarkable similarity between the above and underground magnetic field magnitudes at 50 m (within 5–10%) demonstrates that the magnetic field component experiences minimal medium-dependent attenuation at close range, unlike the electric field components which show order-of-magnitude differences between the above and underground values. This occurs because the magnetic field is determined primarily by the current distribution in the lightning channel itself, with the propagation medium playing a secondary role at distances much smaller than the electromagnetic wavelength.

At $r = 5$ km (far field), the magnetic field magnitudes attenuate to approximately 0.42 to 0.18 A/m — representing attenuation factors of 226$\times$ (Case 2) to 350$\times$ (Case 1) — with peaks occurring at delayed times ($t \approx 17.518$ µs). The ordering of peak magnitudes remains perfectly consistent with both underground far-field and near-field behaviors: Case 2 (first stroke) maintains dominance at approximately 0.42 A/m, followed by Case 3 at approximately 0.32 A/m, Case 5 at approximately 0.25 A/m, Case 4 at approximately 0.22 A/m, and Case 1 at approximately 0.18 A/m. Comparing with underground values at 5 km (Case 2: 0.4 A/m, Case 3: 0.3 A/m), the above-ground magnitudes are nearly identical or slightly higher (within 5–10%), confirming that magnetic field propagation to far distances is relatively independent of whether the observation point is above or below ground surface. The temporal evolution shows characteristic far-field behavior: gradual rise over several microseconds to peaks around $t = 18$–20 µs, followed by very slow decay with Case 2 maintaining approximately 0.40 A/m through $t = 26$ µs. The attenuation factors (226–350$\times$) are slightly more variable than underground (225–300$\times$) but still demonstrate much greater uniformity than the electric field components. The preservation of consistent ordering across all observation locations (underground/above-ground, near-field/far-field) and the strong correlation with peak current magnitude validate the fundamental use of magnetic field measurements for lightning current characterization in location systems and electromagnetic compatibility assessments.

Distance and medium-dependent behaviors reveal several critical insights unique to the magnetic field component. The near-equivalence of the above-ground and underground magnetic field magnitudes at both 50 m (within 5–10%) and 5 km (within 5–10%) stands in stark contrast to the electric field components, which show factors of 7–170$\times$ difference between the above-ground and underground values. This medium independence makes magnetic field measurements more robust and less sensitive to sensor placement height, simplifying the installation requirements for lightning detection systems. The uniform attenuation factors across Cases (226–350$\times$, less than 2$\times$ variation) compared to electric fields (130–3000$\times$, over 20$\times$ variation) demonstrate superior predictability for magnetic field propagation. For overhead power systems and communication lines, the sustained high magnetic fields from the first strokes (Case 2: 95 A/m at 50 m, 0.42 A/m at 5 km) create significant electromagnetic coupling concerns. These fields can induce substantial voltages in elevated conductor loops through magnetic flux linkage, particularly in large loop areas such as distribution line spans or communication cable routes. The direct relationship of the magnetic field to current (through Ampère's law) means that peak magnetic field measurements can provide reliable peak current estimates with typical uncertainties of 15–25%, as demonstrated by the near-linear correlation observed across all Cases (correlation coefficient $r > 0.95$ between peak current and peak H_φ). The consistency of the magnetic field behavior across medium boundaries (air-soil interface) and distance ranges validates its use as the primary field component for lightning location system operation, where accurate current estimation and source location are critical for risk assessment and protection coordination.

The protection zones in Table 2 can be related to the lightning protection levels (LPL I–IV) defined in IEC 62305. For Zone A, fast-rising and severe subsequent strokes (Cases 3–4) govern the design, producing underground electric fields 1.6–2.0$\times$ higher than the baseline subsequent stroke. For Zone C, first return strokes (Case 2) govern, consistent with the high

TABLE 2. Recommended distance-dependent protection design guidelines for lightning electromagnetic fields.

Zone	Distance	Worst-Case Lightning Type	Governing Parameter	Infrastructure Focus
A	< 100 m	Fast-rising subsequent (Case 4) & Severe subsequent (Case 3)	di/dt (80–120 kA/μs)	Buried cables, grounding systems
B	100 m–1 km	Transition zone — both apply	Mixed: di/dt and I_peak	Underground networks, distribution lines
C	> 1 km	First return stroke (Case 2)	Peak current (28 kA)	Overhead transmission lines, regional networks

peak current criteria of IEEE Std 1410. In Zone B, both criteria should be checked and the more conservative result adopted.

4. CONCLUSION

This paper presented a systematic FDTD-based investigation of how lightning current waveform parameters influence radiated electromagnetic fields, comparing five representative lightning types — typical subsequent stroke, first return stroke, severe subsequent stroke, fast-rising subsequent stroke, and rocket-triggered lightning — at near-field ($r = 50$ m) and far-field ($r = 5$ km) distances, both underground ($p = 2$ m) and above ground ($h = 10$ m). The main findings of this study can be summarized as follows:

- ✓ **Distance-dependent transition from di/dt to peak current dominance**. At close range ($r = 50$ m), current rise rate (di/dt) dominates underground electric field components: the fast-rising subsequent stroke (Case 4, 120 kA/μs) produces underground fields comparable to the severe subsequent stroke (Case 3, 80 kA/μs) despite 30% lower peak current, while the first stroke (Case 2, 28 kA) generates moderate underground fields due to its slow rise rate (12 kA/μs). At far distances ($r = 5$ km), peak current magnitude becomes the dominant factor for most field components. Based on the observed behavior between these two distances, the transition is estimated to occur in the 200–500 m range, consistent with the electromagnetic skin depth at frequencies corresponding to the di/dt bandwidth of fast-rising waveforms.

- ✓ **Medium-independence of the azimuthal magnetic field**. The azimuthal magnetic field exhibits unique medium independence, with above-ground and underground values differing by less than 5–10% at both distances — in stark contrast to electric field components that show factors of 7–170× difference between observation heights. Combined with uniform attenuation factors (225–350×) and consistent ordering correlated with peak current across all distances and heights, this medium-independent behavior confirms the suitability of magnetic field measurements for lightning location systems and peak current estimation.

- ✓ **Limitations of triggered lightning as a surrogate for natural lightning**. Triggered lightning (Case 5) underestimates severe natural subsequent strokes by 40–60% in near-field underground electric fields but only 20–30% at far-field distances. This indicates that laboratory experiments using triggered lightning provide better electromagnetic stress representation at regional scales than at close range, and raises an important concern regarding protection standards calibrated on triggered lightning data: such standards may under-represent the worst-Case near-field electromagnetic environment for buried infrastructure within approximately 100 m of a strike point. A reevaluation of triggered-lightning-derived test waveforms for this distance and infrastructure category is recommended.

- ✓ **Distance-zone-based protection design recommendations**. These findings carry direct implications for lightning protection design, summarized in Table 2. Buried infrastructure within approximately 100 m of a lightning strike is most critically threatened by fast-rising and severe subsequent strokes (Cases 3–4), for which di/dt governs transient field coupling. Overhead systems and regional networks at distances beyond 1 km are most critically exposed to first return strokes (Case 2), which maintain the highest above-ground field magnitudes and sustained electromagnetic stress. Protection standards that specify a single worst-case lightning scenario may therefore lead to over-engineering or under-protection depending on infrastructure type and distance; a distance-dependent, waveform-specific approach is necessary for economically optimized and safety-assured protection design.

Future work should prioritize extending the parametric scope of this study to intermediate distances (200 m, 500 m, 1 km, 2 km) to precisely locate the di/dt-to-peak-current transition zone, and to multiple burial depths (0.5 m to 3 m) to cover the full range of buried infrastructure encountered in practice.

REFERENCES

[1] Cooray, V., *The Lightning Flash*, IET Power and Energy Series, 2003.

[2] Cummins, K. L. and M. J. Murphy, "An overview of lightning locating systems: History, techniques, and data uses, with an in-depth look at the U.S. NLDN," *IEEE Transactions on Electromagnetic Compatibility*, Vol. 51, No. 3, 499–518, Aug. 2009.

[3] Yang, Y., Q. Zhou, R. Chen, S. Hou, and X. Bian, "Simulation study of lightning indirect effects on electric vehicle," in *2025 6th International Conference on Electrical, Electronic Information*

and Communication Engineering (EEICE), 479–482, Shenzhen, China, Apr. 2025.

[4] Nicolopoulou, E. P., "Lightning surges in the electric network of a ship: A study with respect to equipment immunity levels," *IEEE Transactions on Transportation Electrification*, Vol. 11, No. 5, 12 159–12 171, Oct. 2025.

[5] Vu, D.-Q., N.-N. Nguyen, T.-M. T. Le, and P.-T. Vu, "Computing lightning-induced voltages on overhead distribution lines using the RBF-FDTD approach," *IEEE Access*, Vol. 13, 125 473–125 484, Jul. 2025.

[6] Chen, R., S. Hou, and Y. Ding, "Numerical simulation analysis of the direct effects of lightning on electric vehicles," in *2025 13th Asia-Pacific International Conference on Lightning (APL)*, 1–6, Bali, Indonesia, Jun. 2025.

[7] Sadique, S., G. Mrudula, A. K. Singh, and S. Varghese, "Study on indirect effects of lightning on aircraft using simulation," in *2025 IEEE Space, Aerospace and Defence Conference (SPACE)*, 1–6, Bangalore, India, Jul. 2025.

[8] Hou, S., Y. Zhou, Y. Ding, T. Xu, Y. Zhang, and R. Chen, "A review of lightning protection technologies for electric vehicles," in *2025 2nd International Conference on Electrical Technology and Automation Engineering (ETAE)*, 542–548, Guangzhou, China, May 2025.

[9] Tarimer, I. and B. Kuca, "An overview on the protection measures for air-port protection in high density lightning regions," *Elektronika ir Elektrotechnika*, Vol. 19, No. 10, 29–32, 2013.

[10] Tarimer, I., B. Kuca, and T. Kisielewicz, "A case study to risk assessment for protecting airports against lightening," *Elektronika Ir Elektrotechnika*, Vol. 117, No. 1, 49–52, 2012.

[11] Tarimer, I., C. Mazzetti, B. Kuca, and Z. Flisowski, "Considerations on efficiency for internal lightning protection," *Advances in IT and Electrical Engineering*, Vol. 22, No. 33, 277–285, 2013.

[12] Tarimer, I. and B. Kuca, "The proposition to safety of a lightning protection system for high structures," *TEM Journal*, Vol. 2, No. 4, 309–313, 2013.

[13] Mimouni, A., F. Rachidi, and M. Rubinstein, "Electromagnetic fields of a lightning return stroke in presence of a stratified ground," *IEEE Transactions on Electromagnetic Compatibility*, Vol. 56, No. 2, 413–418, 2014.

[14] Omari, M. and A. Mimouni, "Electromagnetic fields at very close range from a tower struck by lightning in presence of a horizontally stratified ground," *IEEE Transactions on Electromagnetic Compatibility*, Vol. 61, No. 1, 166–173, 2019.

[15] Omari, M. and A. Mimouni, "Electromagnetic fields at far distances from the peissenberg tower struck by lightning in presence of a horizontally stratified ground," in *2018 34th International Conference on Lightning Protection (ICLP)*, 1–7, Rzeszow, Poland, Sep. 2018.

[16] Omari, M. and I. Ghlib, "The vertical stratification (mixed propagation path: Land-lake) effect on the electromagnetic fileds of lightning initiated to the CN tower," in *2022 2nd International Conference on Advanced Electrical Engineering (ICAEE)*, 1–5, Constantine, Algeria, Oct. 2022.

[17] Omari, M., A. Mimouni, and I. Ghlib, "FDTD modeling of lightning electromagnetic fields over mixed and sloped domains using staircase approximation," *Progress In Electromagnetics Research B*, Vol. 112, 29–41, 2025.

[18] Li, Q., M. Rubinstein, J. Wang, L. Cai, M. Zhou, Y. Fan, and F. Rachidi, "On the influence of the soil stratification and frequency-dependent parameters on lightning electromagnetic fields," *Electric Power Systems Research*, Vol. 178, 106047, Jan. 2020.

[19] Rachidi, F., W. Janischewskyj, A. M. Hussein, C. A. Nucci, S. Guerrieri, B. Kordi, and J.-S. Chang, "Current and electromagnetic field associated with lightning-return strokes to tall towers," *IEEE Transactions on Electromagnetic Compatibility*, Vol. 43, No. 3, 356–367, Aug. 2001.

[20] Rakov, V. A. and M. A. Uman, *Lightning: Physics and Effects*, Cambridge University Press, 2003.

[21] Nag, A., M. J. Murphy, W. Schulz, and K. L. Cummins, "Lightning locating systems: Insights on characteristics and validation techniques," *Earth and Space Science*, Vol. 2, No. 4, 65–93, 2015.

[22] Rakov, V. A., M. A. Uman, and R. Thottappillil, "Review of lightning properties from electric field and TV observations," *Journal of Geophysical Research: Atmospheres*, Vol. 99, No. D5, 10 745–10 750, 1994.

[23] Yee, K., "Numerical solution of initial boundary value problems involving Maxwell's equations in isotropic media," *IEEE Transactions on Antennas and Propagation*, Vol. 14, No. 3, 302–307, May 1966.

[24] Mur, G., "Absorbing boundary conditions for the finite-difference approximation of the time-domain electromagnetic-field equations," *IEEE Transactions on Electromagnetic Compatibility*, Vol. 23, No. 4, 377–382, Nov. 1981.

[25] Visacro, S. and R. Alipio, "Frequency dependence of soil parameters: Experimental results, predicting formula and influence on the lightning response of grounding electrodes," *IEEE Transactions on Power Delivery*, Vol. 27, No. 2, 927–935, Apr. 2012.

[26] Heidler, F., "Analytic lightning current functions for LEMP calculations," in *18th International Conference on Lightning Protection (ICLP)*, 63–66, Munich, Germany, 1985.

[27] Nucci, C. A., C. Mazzetti, F. Rachidi, and M. Ianoz, "On lightning return stroke models for LEMP calculations," in *19th International Conference on Lightning Protection*, 463–469, 1988.

[28] Rachidi, F. and C. A. Nucci, "On the Master, Uman, Lin, Standler and the modified transmission line lightning return stroke current models," *Journal of Geophysical Research: Atmospheres*, Vol. 95, No. D12, 20 389–20 393, Nov. 1990.